Results in Chemistry 6 (2023) 101216

Contents lists available at ScienceDirect

Results in Chemistry

journal homepage: www.sciencedirect.com/journal/results-in-chemistry

One-step electrodeposition of NiS heterostructures on nickel foam electrodes for hydrogen evolution reaction: On the impact of thiourea content

Ioannis A. Poimenidis [a,*], Maria Lykaki [a], Nikandra Papakosta [b,c], Panagiotis A. Loukakos [b], Nikolaos Kallithrakas Kontos [d], Michalis Konsolakis [a,*]

[a] Technical University of Crete, School of Production Engineering & Management, Lab of Matter Structure and Laser Physics, 73100 Chania, Crete, Greece
[b] Foundation for Research and Technology – Hellas, Institute of Electronic Structure and Laser, 70013 Heraklion, Greece
[c] University of Crete, Department of Materials Science and Technology, 70013 Vassilika Vouton, Heraklion, Greece
[d] Technical University of Crete, Laboratory of Analytical and Environmental Chemistry, University Campus, Chania, Greece

ARTICLE INFO

Keywords:
Alkaline electrolysis
HER reaction
Electrodeposition on Ni foam
Nickel sulfide heterostructures
Thiourea

ABSTRACT

Herein, we report on the one-step growth of nickel sulfide (NiS) heterostructures on nickel foam (NF) substrate via a facile electrodeposition method, employing $Ni(NO_3)_2{\cdot}6H_2O$ and CH_4N_2S as Ni and S precursors, respectively. For the first time, a systematic study was carried out on the impact of the Ni/S molar ratio on the electrochemical performance of as-prepared electrodes for water splitting. The optimum performance was obtained for a Ni:S ratio equal to 2:1, whereas lower or higher ratios resulted in much inferior performance. The NiS@NF electrode with a Ni:S ratio of 2:1 exhibited the lowest overpotentials $|\eta_{10}| = 136$ mV, $|\eta_{100}| = 209$ mV, extremely low Tafel slope (60 mV dec^{-1}), and very high double layer capacitance value (2.78 mF cm^{-2}). Field emission scanning electron microscopy (FE-SEM), X-ray diffraction (XRD), X-ray fluorescence spectroscopy (XRF), and X-ray photoelectron spectroscopy (XPS) revealed the formation of a coral-like nanoarchitecture, resulting in enhanced HER activity.

Introduction

The high global demand for energy consumption and the calls for the transition to green energy led to the search for alternative energy sources such as solar, wind, water, and hydrogen [1,2]. Hydrogen production could be pollution-free, independent of the timescale and the weather, and act as a secure and clean energy carrier [3,4].

Generally, industrial water-splitting devices operating in an alkaline medium have gained particular attention toward producing H_2 and O_2 [5]. Most of these devices use Pt-based porous nanomaterials because of their superior electrochemical performance for hydrogen evolution reaction (HER). However, their scarcity and high cost hinder their practical application, rendering essential the turn into the rational design of cost-efficient and highly active non-precious metal HER electrodes [6]. Among the different candidates, transition metal sulfides (TMS) have gained particular attention due to their high electrical conductivity, ideal atomic arrangement, and intrinsic electrocatalytic activity for HER [7,8]. Moreover, according to recent studies, sulfur vacancies optimize the hydrogen adsorption-free energy (ΔG_H) [9]. Several studies have explored TMS for HER, such as MoS_2 fabricated with chemical vapor deposition and spin-coated for alkaline and neutral electrolytes [7], $MoS_2/Fe_5Ni_4S_8$ fabricated with a 2-step hydrothermal process for alkaline solutions [10], Ni_2S_3 with the addition of $C_6H_5O_7Na_3$ for better adhesion[11], NiS@$CuBi_2O_4$ via the one-pot electrochemical method and cyclic voltammetry[12], NiS/Ni on carbon cloth via solvothermal method presenting a very low Tafel slope[13], and hollow Chevrel-Phase $NiMo_3S_4$ fabricated with a template-directed anion exchange pathway [14]. Moreover, He et al. [15] explored the impact of various applied current densities during electrodeposition of sulfur layers on NF, while Edison et al. [16] prepared a NiS@NF electrode to act as an anode in a hybrid-capacitor system with promising results.

Although various studies have been devoted to the transition metal sulfides with satisfying results, there is no a systematic study on the influence of sulfur/metal atomic ratio during the preparation procedure, which is expected to affect the structural and electrochemical properties notably and, in turn, the HER efficiency. In addition, although

* Corresponding authors.
E-mail addresses: ipoimenidis@tuc.gr (I.A. Poimenidis), mkonsolakis@tuc.gr (M. Konsolakis).

https://doi.org/10.1016/j.rechem.2023.101216
Received 23 October 2023; Accepted 14 November 2023
Available online 15 November 2023

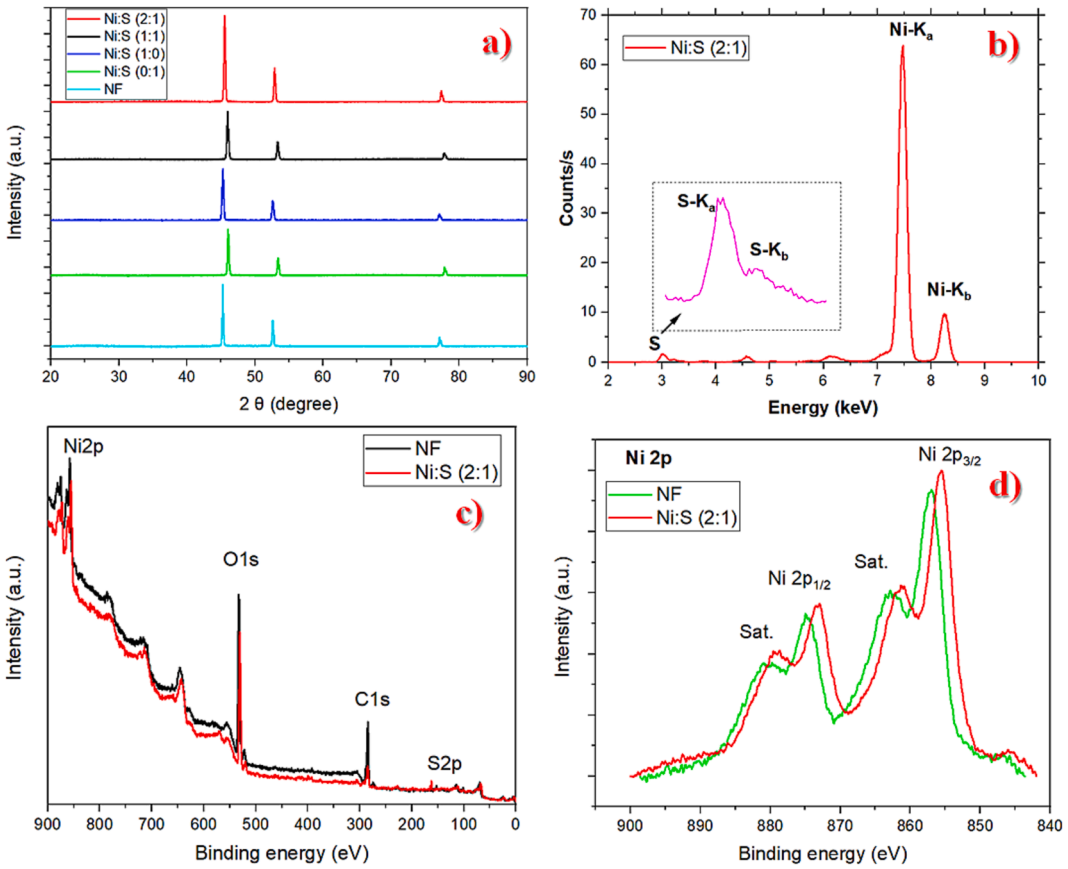

Fig. 1. XRD analysis (a), XRF analysis (b), XPS survey pattern (c), XPS Ni2p spectra (d) of the NF, Ni:S (1:0), Ni:S (0:1), Ni:S (1:1), Ni:S (2:1) electrodes.

satisfactory results have been obtained with the aforementioned TMS, the multi-step and the time-consuming fabrication procedures followed in most cases further hamper their widespread applicability.

Motivated by these issues, a one-step electrodeposition process was applied to fabricate NiS_x heterostructures with different Ni:S atomic ratios, employing $Ni(NO_3)_2{\cdot}6H_2O$ and Thiourea as Ni and S sources. In this regard, the novelty and originality of the present work rely on the systematic impact of the Ni/S atomic ratio on HER efficiency, which, to the best of our knowledge, has not yet been explored. Interestingly, neither Ni-rich nor S-rich electrodes performed satisfactorily, revealing the importance of adjusting the metal/sulfur ratio. It was clearly disclosed that the Ni:S ratio could profoundly influence the electrochemical performance by optimizing the Ni:S ratio to 2:1, which offers a very low Tafel slope (60 mV dec^{-1}), low overpotentials, and enhanced C_{DL} value (2.78 mF cm^{-2}).

Experimental details

Materials and reagents

All the chemical reagents in this work were used as received without further purification. Thiourea (CH_4N_2S, 98 % Penta Chemical), nickel nitrate hexahydrate ($Ni(NO_3)_2{\cdot}6H_2O$, 99 % Sigma-Aldrich), potassium hydroxide (KOH, technical grade, Sigma-Aldrich), ethanol (CH_3CH_2OH 99.8 %, ACROS Organics), hydrochloric acid (HCl 98 % Sigma Aldrich). Nickel foam (99.8 %, Beike advanced materials Store).

Electrodeposition on Ni foam

All the fabricated NF electrodes were electrodeposited with chronoamperometry using a Princeton Applied Research electrochemical station (VersaSTAT 4) in a standard three-electrode electrochemical cell. The electrochemical cell was equipped with a pure Pt (99.9 %) (Goodfellow) counter electrode and an Ag/AgCl (3.5 M KCl) (Palmsens) reference electrode equipped with a Luggin capillary. The NF substrate acted as the working electrode.

Before the electrodeposition, the working electrode (NF) was ultrasonicated in 3 M HCl to remove organic contaminations from its surface and activate the substrate [17]. Afterward, it was rinsed with deionized water, ultrasonicated in pure ethanol, and finally rinsed again with deionized water.

The deposition time was 10 min, at 298 K, for all the fabricated electrodes. The applied potential varied from −0.18 to −0.2 V vs. RHE, in order to avoid hydrogen mass production, resulting in poor electrodeposition on the NF substrate, as well as to overcome the low conductivity of the sulfur-rich solution . Also, a magnetic stirrer was used for uniform deposition. Thiourea and $Ni(NO_3)_2{\cdot}6H_2O$ compounds were used as precursors of Ni and S, respectively, in a wide range of Ni:S molar ratios, i.e., 1:0, 0:1, 1:1, 2:1, 4:1, 1:2 and 1:4. For comparison purposes pure Ni (1:0) and S (0:1) electrodes on NF substrate were fabricated. Finally, all the fabricated electrodes were heated at 573 K for two hours to decompose the precursor compounds and to increase the electrodes' crystallinity and stability [18–20].

Structural characterization and chemical analysis

The fabricated Ni foam electrodes were morphologically characterized with field emission scanning electron microscopy (FE-SEM, JSM7000F, JEOL) at various magnification scales. Also, XRD (BEDE D1 with CuKa radiation), XPS analysis (SPECS, FlexMod XPS), and XRF (Amptek X-123) analyses were carried out to gain insight into the structural features and chemical composition of the NiS@NF electrodes.

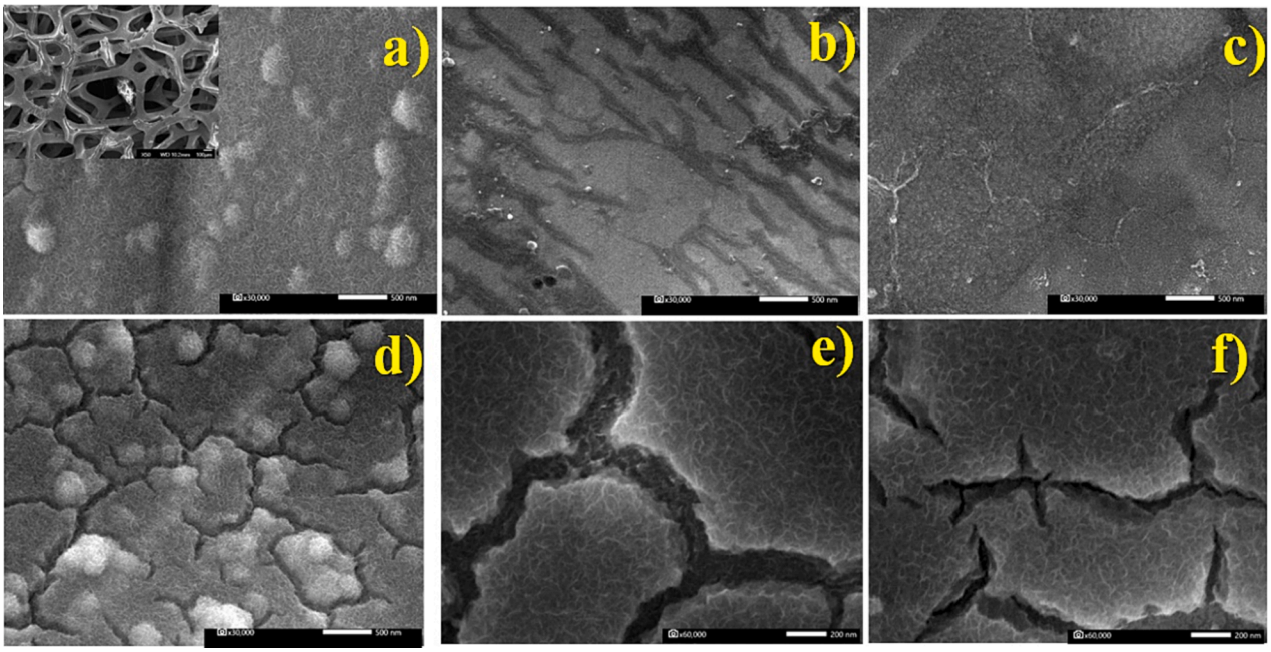

Fig. 2. FE-SEM of the Ni:S (1:0) (a) inset NF, Ni:S (0:1) (b), Ni:S (1:1) (c), Ni:S (2:1) (d), Ni:S (2:1) higher magnification scale (e, f).

Electrochemical evaluation

The electrochemical evaluation of the electrodeposited NF electrodes was studied by cyclic voltammetry (CV), linear sweep voltammetry (LSV), Tafel slope, double layer capacitance values (C_{DL}), electrochemical active surface area (ECSA), and electrochemical impedance spectroscopy (EIS). The VersaSTAT 4 electrochemical workstation was used for the electrochemical analysis of the fabricated NiS@NF electrodes. The electrochemical cell was equipped with a pure Pt (99.9 %) (Goodfellow) counter electrode and an Ag/AgCl (3.5 M KCl) (Palmsens) reference electrode, while the fabricated NF electrodes acted as working electrodes. The electrolyte for the electrochemical measurements was a 1 M KOH solution. Before each experiment, N_2 gas was purged into the cell to remove the dissolved oxygen gas. All the experiments were repeated at least three times to confirm the obtained results. In addition, all potential values in this manuscript are converted to a reversible hydrogen electrode (RHE) with the equation $E_{RHE} = E_{Ag/AgCl} + 0.059 \cdot pH + E_{o\ Ag/AgCl}$

where $E_{Ag/AgCl}$ is the potential measured with Ag/AgCl reference electrode.

In the sections below, the samples with Ni:S ratios of 1:2, 1:4, and 4:1 are not included for brevity's shake and are included in the supplementary information (SI), considering that their electrochemical performance is similar or inferior to the rest of the samples.

Results and discussion

Electrodeposition

During electrodeposition, the electrochemical reaction and diffusion rate mainly control the overall process. When the diffusion rate is faster than the reaction rate, the electrodeposition is governed by the electrochemistry reaction. On the other hand, if the diffusion rate is slower than the reaction rate, the diffusion controls the electrodeposition [21].

During the electrodeposition process in the current work, the mixture of Ni^{2+} and thiourea solution produces a stable nickel-thiourea complex, which afterward is reduced to insoluble heterostructures of NiS on the NF surface, according to the following reaction scheme [16,22–24]:

$$2H_2O + 2e^- \rightarrow 2OH^- + H_2 \quad (1)$$

$$CH_4N_2S + 2OH^- \rightarrow S^{2-} + CON_2H_4 + H_2O \quad (2)$$

$$Ni^{2+} + S^{2-} \rightarrow NiS \quad (3)$$

In this work, the temperature was held constant (298 K) during electrodeposition, and the distance of the electrodes was set at 3 mm.

Structural/morphological characterization

Fig. 1a depicts the XRD patterns of representative electrodes, i.e., bare NF and NiS@NF samples with Ni:S ratio of 0:1 (pure S), 1:0 (pure Ni), 1:1, and 2:1. The XRD analysis of the fabricated electrodes (Fig. 1a) shows three major peaks for the pure nickel foam (NF) and for the sample without Thiourea, i.e., Ni:S (1:0) at the 2θ angle of 45.2°, 52.5° and 77°, which correspond to the (111), (200) and (220) planes of crystalline Ni [16]. These results verify the metallic nature of Ni before and after the electrodeposition in nickel foam. However, in the case of thiourea-doped electrodes, the Ni peaks were shifted to higher angles 46°, 53.50°, and 77.8°, which are attributed to (102), (110), and (202) crystalline planes of NiS, respectively (JCPDS file No. 02–1280)[25,26]. Furthermore, the FWHM of sulfur-doped electrodes is higher than the NF sample, suggesting the successful formation of NiS phase on the NF substrate, in line with the literature [16].

The crystallite size was also calculated by applying the Scherrer equation. The smallest crystallite size of 28 nm was obtained for Ni:S (2:1), followed by the Ni:S (1:1) sample, which obeys a size of 29 nm. All other samples exhibit a higher crystallite size varying between 31 and 34 (Table S1). Since the samples with smaller crystallite sizes also demonstrated the optimum electrochemical performance (see below), this could imply a structure-performance relationship; smaller crystallite sizes with higher lattice strain result in more active sites (Table S1), thus improving the HER performance in accordance with relevant studies [27–29].

The successful formation of NiS heterostructures was further confirmed by the XRF and XPS analysis (Fig. 1) over the NiS (2:1) electrode, which exhibits the best electrochemical performance (see below). In particular, XRF analysis indicates the presence of S and Ni,

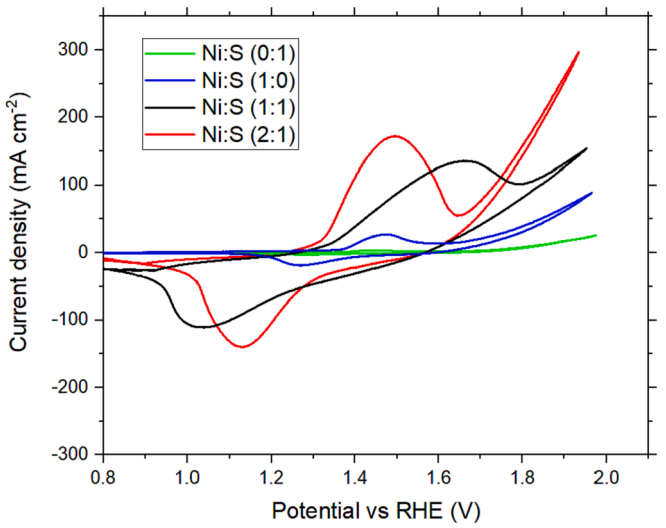

Fig. 3. Cyclic voltammograms of Ni:S (1:0), Ni:S (0:1), Ni:S (1:1), Ni:S (2:1) electrodes with 100 mVs^{-1} sweep rate in 1 M KOH.

further supporting the XRD results (Fig. 1b). Also, the XPS spectra of bare NF and Ni:S (2:1) samples are presented comparatively in Fig. 1c, d. The NiS heterostructure creation on the NF substrate was further supported by the shift of Ni2p peaks to lower binding energies since the electronegativity of sulfur is higher than nickel [30].

The surface area and morphology of the fabricated electrodes, which play a pivotal role in the electrochemical performance, are analyzed by FE-SEM (Fig. 2). In the S-free Ni:S (1:0) sample, a dense electrode surface is obtained without any apparent cracks (Fig. 2a). However, as the molar ratio of Ni:S increases cracks are starting to appear on the entire electrode's surface. These cracks are more evident at Ni:S (2:1) (Fig. 2d, e), resulting in a coral-like protrusion morphology. The internal stress of Ni foam and NiS doping during the electrodeposition is most probably responsible for the produced cracks, as also postulated in previous relevant studies [25]. Also, considering Fig. 2d, the surface microstructure of Ni:S (2:1) consists of a bulky crystalline core and ultra-thin nanowires attached to every crack, providing a higher electrochemical area with more effective active sites for electrocatalysis [26,27]. Similar morphologies have been previously observed upon increasing the content of Thiourea over Ni@NF, attributed to the formation of bubbles and the difference in internal stress of Ni and NiS during the electrochemical deposition [11].

Electrochemical performance

In Fig. 3, the cyclic voltammograms of Ni:S (2:1), Ni:S (0:1), Ni:S (1:1), and Ni:S (1:0) samples are depicted. Well-defined redox peaks appeared, indicating the Faraday reaction nature of the NiS@NF electrode [31].

The reaction of nickel sulfides in an alkaline medium can be expressed through the equation[32–34]:

$$NiS + OH^- \leftrightarrow NiSOH + e^- \quad (4)$$

Generally, the enclosed area of the CV curves can be used as the first estimation of specific capacitance, whereas the maximum value of current density peaks (J_{peak}) can be correlated with the electrochemically active surface area (ECSA) [35–37]. Interestingly, the Ni:S (2:1) sample exhibits the largest enclosed area and the highest J_{peak}, implying that a Ni:S ratio 2:1 results in the maximum specific capacitance and ECSA, in line with its structural and morphological characteristics.

Cathodic polarization curves (0 to −0.4 V vs. RHE) were obtained (Fig. 4a, S1, and Table 1) with a sweep rate of 1 mVs^{-1} to explore the overpotential values and to gain insight into electrode kinetics. Considering Fig. 4a, it is evident that electrodes with only S deposition (Ni:S (0:1)) exhibit inferior catalytic activity. In contrast, the NiS@NF electrodes of various molar ratios (Figs. 4 and S1) demonstrated much lower overpotential values. Considering the impact of thiourea content, similar phenomena have been observed by Huijuan Jing et al. [38], where large sulfur ratios decrease HER efficiency.

It is evident from Fig. 4a and S1 (involving the whole range of Ni:S ratios investigated) that the best electrochemical values, summarized in Table 1, can be obtained with the NiS@NF sample with a Ni:S molar ratio of 2:1. In particular, the overpotential value at current density 10 mA cm^{-2} ($|\eta_{10}|$) of the Ni:S (2:1) is the lowest (0.136 V) compared to all the other fabricated electrodes. Moreover, a stability test was performed for the Ni:S (2:1) electrode in 1 M KOH electrolyte for 12 h (Fig. S2), demonstrating its adequate stability.

Moreover, the HER mechanism was investigated by considering the

Table 1
Electrochemical values for the NiS@NF fabricated electrodes in 1 M KOH.

Electrode	$\eta\|_{10}\|$ (V)	Tafel slope b (mV dec^{-1})
NF	0.31	128 ± 0.8
Ni:S (0:1)	0.27	181 ± 1.5
Ni:S (1:4)	0.21	165 ± 0.8
Ni:S (1:2)	0.19	135 ± 0.4
Ni:S (1:1)	0.18	113 ± 0.3
Ni:S (2:1)	0.13	60 ± 0.5
Ni:S (4:1)	0.17	131 ± 0.6
Ni:S (1:0)	0.2	119 ± 0.4

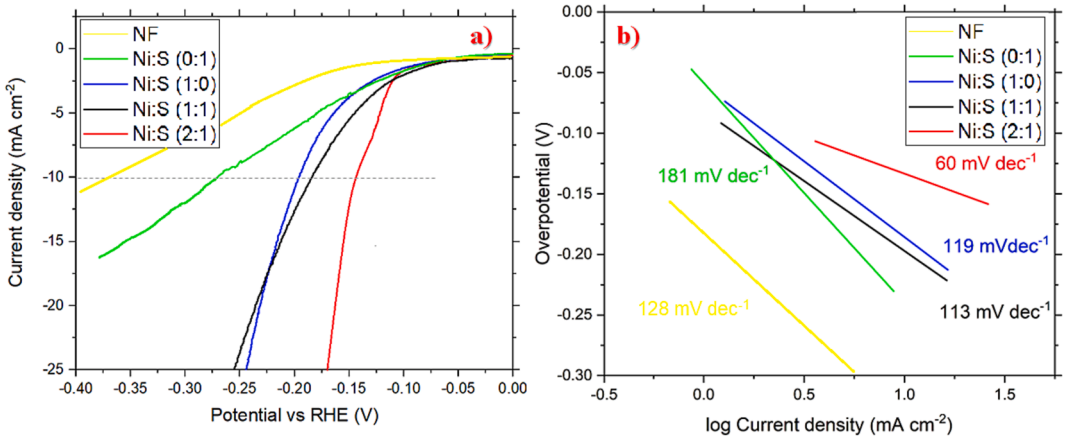

Fig. 4. Polarization curves (a) and Tafel slopes (b) for the NF (reference), Ni:S (1:0), Ni:S (0:1), Ni:S (1:1), Ni:S (2:1) electrodes in 1 M KOH.

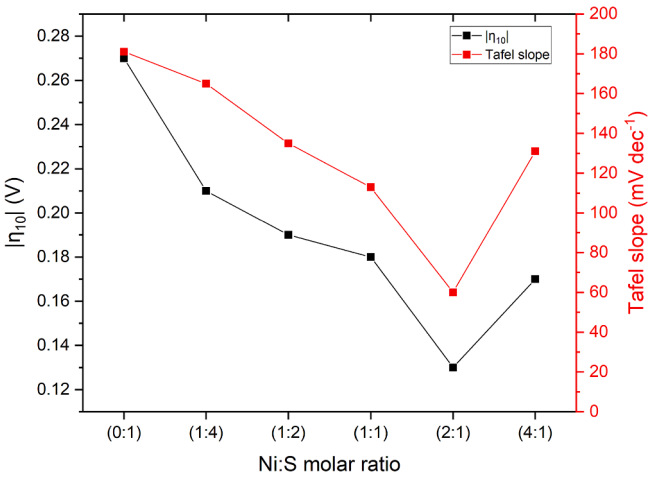

Fig. 5. Ni:S molar ratio vs $|n_{10}|$ and Tafel slope values.

Tafel slope (Table 1), which is calculated by plotting the overpotential value vs. the logarithm of the current density. As depicted in Fig. 4b and S3, the Ni:S ratio of 2:1 results in an ultra-low Tafel slope of 60 mV dec^{-1}, which is among the lowest in literature (Table S2), implying its enhanced HER kinetics [39–41].

The pivotal role of the Ni:S ratio on the electrochemical performance is more clearly demonstrated in Fig. 5, which portrays the $|n_{10}|$ and Tafel slope values as a function of the Ni:S ratio. It is evident that the lowest $|n_{10}|$ and Tafel slope values are obtained for a Ni:S ratio of 2:1, whereas either Ni-rich (Ni:S > 2) or S-rich (Ni:S < 2) results in a much inferior performance.

The improved electrochemical performance of NiS@NF composites with an adjustable Ni:S ratio can be attributed to the synergistic effects of Ni-NiS heterostructures towards an enhanced HER kinetics via the Volmer – Heyrovsky mechanism [11,42]. Specifically, in an alkaline solution, the hydrogen evolution reaction can be described by the following elementary steps [11,42,43]:

The Volmer reaction (discharge step) with a Tafel slope around 118 mV dec^{-1}:

$$H_2O + e^- \rightarrow H_{ads} + OH^- \quad (5)$$

and the Heyrovsky reaction (desorption step) with a Tafel slope around 40 mV dec^{-1}:

$$H_{ads} + H_2O + e^- \rightarrow H_2 + OH^- \quad (6)$$

or the Tafel recombination reaction with Tafel slope around 30 mV dec^{-1}:

$$2H_{ads} \rightarrow H_2 \quad (7)$$

The decreased Tafel slope of the Ni:S electrodes indicates that the Volmer reaction is notably accelerated towards producing more H_{ads} and OH^- species. This could be attributed to the fine-tuning of electron configuration around the active electrocatalytic sites via the formation of Ni@NiS heterostructures, which facilitates the H_{ads} and OH^- bonding to active sites, thus lowering the energy barrier for H_2O splitting via the Volmer reaction [6,11,44].

To gain insight into the different electrocatalytic properties of each electrode, the C_{DL} and ECSA values were next calculated through the cyclic voltammetry method. Various scan rates (5 to 100 mVs^{-1}) were applied around the open circuit potential (±50 mV) in a non-Faradaic region (Fig. S4) to calculate the C_{DL} values [4,45,46]. C_{DL} values obtained by the cyclic voltammetry method are proportional to the dependent capacitive current (J_{DL}) of the fabricated electrodes through the following equation [46–49]:

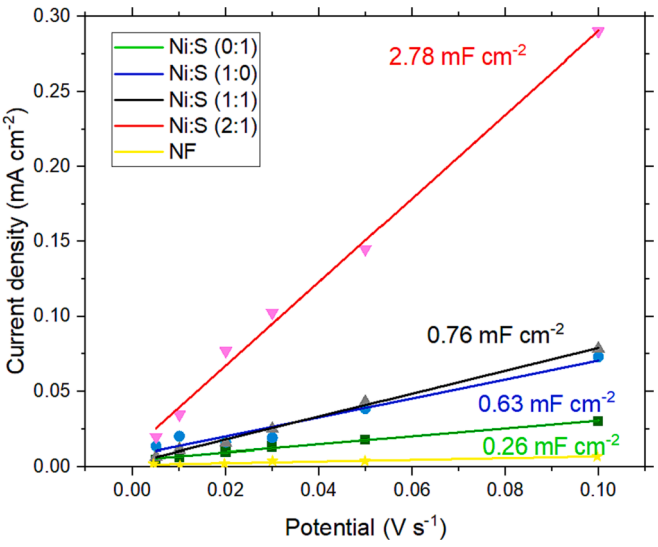

Fig. 6. Average absolute current density vs. scan rate of NF, Ni:S (0:1), Ni:S (1:0), Ni:S (1:1), Ni:S (2:1) electrodes in 1 M KOH, at scan rates 0.005 V s^{-1} – 0.1 V s^{-1}.

Table 2
C_{DL} values obtained with the cyclic voltammetry method at scan rates 0.005 V s^{-1} – 0.1 V s^{-1}, calculated ECSA and S_A for the NiS@NF electrodes.

Electrode	C_{DL} values (mF cm^{-2})	ECSA (cm^{-2})	S_A
NF	0.23 ± 0.02	11.5 ± 0.6	$0.2*10^{17}$
Ni:S (0:1)	0.26 ± 0.01	13 ± 0.5	$0.25*10^{17}$
Ni:S (1:4)	1.85 ± 0.23	92.5 ± 1.8	$8.5*10^{17}$
Ni:S (1:2)	1.01 ± 0.05	50.5 ± 0.6	$4.3*10^{17}$
Ni:S (1:1)	0.76 ± 0.02	38 ± 0.8	$4*10^{17}$
Ni:S (2:1)	2.78 ± 0.09	139 ± 1.1	$9.6*10^{17}$
Ni:S (4:1)	2.02 ± 0.12	101 ± 1.5	$8.8*10^{17}$
Ni:S (1:0)	0.63 ± 0.07	31.5 ± 0.6	$1.3*10^{17}$
Perfectly smooth Ni electrode	0.02 ± 0.004	1 ± 0.2	

$$J_{DL} = C_{DL} \times \frac{v}{A} \quad (8)$$

where v stands for scan rate (V s^{-1}) and A for the electrode surface (cm^2).

Fig. 6 depicts the current density as a function of scan rate for Ni:S (0:1), Ni:S (1:0), Ni:S (1:1), Ni:S (2:1) electrodes, whereas the corresponding results for the rest electrodes are presented in Fig. S5. The obtained C_{DL} values for all electrodes are summarized in Table 2.

It is evident that the Ni:S (2:1) exhibits by far the maximum C_{DL} value (2.78 mF cm^{-2}) compared to all the other fabricated electrodes, also possessing the higher ECSA, which is related to the population of exposed active sites and thus improved HER efficiency [50,51]. It should also be mentioned that the obtained C_{DL} values of the Ni:S (2:1) are comparable to those of electrodes used for battery-type or hybrid capacitors [16,37].

In order to extract the ECSA value of each electrode (Table 2) and to directly correlate the HER performance with the exposed active sites of the electrode's surface, the following equation was used:

$$ECSA = C_{DL}/20 \quad (9)$$

The value 20 μF cm^{-2} is the C_{DL} value of a perfectly smooth Ni electrode [52–54]. The highest ECSA value of the Ni:S (2:1), i.e., 139 cm^{-2}, could be attributed to porous morphology (Fig. 2d) and the excellent conductivity obtained by the 2:1 ratio. The multichannel-created porous-

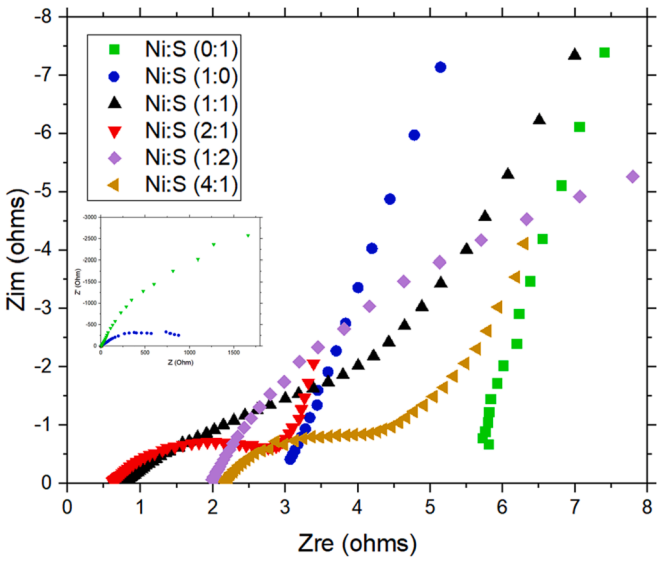

Fig. 7. Zoom in Nyquist plot of Ni:S (0:1), Ni:S (1:0), Ni:S (1:1), Ni:S (2:1), Ni:S (1:2), and Ni:S (4:1) electrodes in 1 M KOH. Inset: Nyquist plot zoomed out.

Table 3
Elemental values of fitted equivalent circuits obtained by EIS.

Electrode	R_{ct} (Ω)	R_s (Ω)
Ni:S (0:1)	8511 ± 802	5.34 ± 0.08
Ni:S (1:0)	1059 ± 40	2.7 ± 0.06
Ni:S (1:1)	8.7 ± 1	0.68 ± 0.007
Ni:S (2:1)	2.1 ± 0.04	0.58 ± 0.004
Ni:S (1:2)	7.8 ± 0.6	1.9 ± 0.03
Ni:S (4:1)	2.5 ± 0.05	2.13 ± 0.006

branch-like structures increased the surface area and accessed more hydroxyl ions, resulting in higher ECSA values [55].

To further investigate the active electrocatalytic area of the aforementioned electrodes, the number of accessible active sites was calculated (equation 10) since an abundant number of them enhances the electrical conductivity of the electrode [56,57].

$$S_A = (\text{integrated reduction area/scan rate})/\text{charge of one electron} \quad (10)$$

where S_A stands for accessible active sites, the scan rate was 100 mV s^{-1}, and the charge of one electron is 1.60217· 10^{-19}C. Considering Table 2, the highest number of SA is attained for the Ni:S (2:1) electrode, implying its improved electrical conductivity and, thus, HER activity.

In Fig. 7, the Nyquist plots of the fabricated electrodes are presented to further investigate the electrochemical kinetics through electrochemical impedance spectroscopy (EIS). The frequency range was 10 mHz to 10 kHz with an alternate signal (RMS) of 10 mV.

The interception of each line with the Z real axis (at high frequency) corresponds to the electrolyte's electronic resistance combined with the electrode's internal resistance (R_s) [58–60]. The constant phase element (CPE) represents the double-layer capacitance between solid and ionic solutions [61], while R_{ct} is the charge transfer resistance, which is the rate of charge exchange between the electrode and the electrolyte interface [62].

Notably, the Ni- and S-containing electrodes with NiS heterostructures exhibit much lower R_s and R_{ct} values compared to bare Ni (Ni:S (1:0)) or bare S (Ni:S (0:1)) electrodes (Table 3), implying the synergistic Ni-S effects towards faster HER kinetics. The optimum values, especially of R_{ct}, were obtained for the Ni:S (2:1) electrode, implying its high conductivity towards improving the charge transfer and the HER efficiency [63,64]. Moreover, the lowest R_s values obtained for the Ni:S (2:1) electrode imply its low resistance at the electrode and electrolyte interface.

Conclusion

The present work systematically explored the impact of the Ni/S molar ratio on the HER efficiency in an alkaline medium over NiS@NF electrodes. CH_4N_2S and $Ni(NO_3)_2{\cdot}6H_2O$ compounds were used as Ni and S precursors at different molar ratios to fabricate NiS heterostructures on a nickel foam substrate through electrodeposition.

It was found that the Ni:S molar ratio profoundly influences the structural/morphological characteristics and, in turn, the HER efficiency. The optimum electrochemical results were obtained for the Ni:S ratio of 2:1, which offers a C_{DL} value of 2.78 mF cm^{-2}, accompanied by a very low Tafel slope of 60 mV dec^{-1} and a low overpotential value at 10 mA cm^{-2} (0.136 V). Moreover, EIS revealed its superior conductivity, which can be accounted for by the improved charge transfer and HER kinetics. Structural and morphological characterization clearly disclosed the formation of NiS heterojunctions over nickel foam, which is conducive for cracks formation of coral-like morphology, thus improving the active electrochemical area for hydrogen evolution.

Declaration of Competing Interest

The authors declare that they have no known competing financial interests or personal relationships that could have appeared to influence the work reported in this paper.

Data availability

Data will be made available on request.

Acknowledgment

The authors want to acknowledge Ms. A. Manousaki for the field emission SEM.

PL, NP acknowledge financial support from the European Union's Horizon 2020 research and innovation program under grant agreement no 871124 Laserlab-Europe. The authors would like to acknowledge the HELLAS-CH national infrastructure (MIS 5002735) implemented under "Action for Strengthening Research and Innovation Infrastructures," funded by the Operational Programme" Competitiveness, Entrepreneurship, and Innovation" (NSRF 2014-2020) and co-financed by Greece and the European Union (European Regional Development Fund).

Appendix A. Supplementary data

Supplementary data to this article can be found online at https://doi.org/10.1016/j.rechem.2023.101216.

References

[1] X. Peng, Y. Yan, X. Jin, C. Huang, W. Jin, B. Gao, et al., Recent advance and prospectives of electrocatalysts based on transition metal selenides for efficient water splitting, Nano Energy 78 (2020), 105234, https://doi.org/10.1016/j.nanoen.2020.105234.

[2] D. Siegmund, N. Blanc, M. Smialkowski, K. Tschulik, U. Apfel, Metal-Rich Chalcogenides for Electrocatalytic Hydrogen Evolution: Activity of Electrodes and Bulk Materials, ChemElectroChem 7 (2020) 1514–1527, https://doi.org/10.1002/celc.201902125.

[3] I. Staffell, D. Scamman, A. Velazquez Abad, P. Balcombe, P.E. Dodds, P. Ekins, et al., The role of hydrogen and fuel cells in the global energy system, Energ. Environ. Sci. 12 (2019) 463–491, https://doi.org/10.1039/C8EE01157E.

[4] C.C.L. McCrory, S. Jung, J.C. Peters, T.F. Jaramillo, Benchmarking Heterogeneous Electrocatalysts for the Oxygen Evolution Reaction, J. Am. Chem. Soc. 135 (2013) 16977–16987, https://doi.org/10.1021/ja407115p.

[5] C.C.L. McCrory, S. Jung, I.M. Ferrer, S.M. Chatman, J.C. Peters, T.F. Jaramillo, Benchmarking Hydrogen Evolving Reaction and Oxygen Evolving Reaction Electrocatalysts for Solar Water Splitting Devices, J. Am. Chem. Soc. 137 (2015) 4347–4357, https://doi.org/10.1021/ja510442p.

[6] J. Yin, J. Jin, H. Zhang, M. Lu, Y. Peng, B. Huang, et al., Atomic Arrangement in Metal-Doped NiS 2 Boosts the Hydrogen Evolution Reaction in Alkaline Media, Angew. Chem. Int. Ed. 58 (2019) 18676–18682, https://doi.org/10.1002/anie.201911470.

[7] G. Li, D. Zhang, Y. Yu, S. Huang, W. Yang, L. Cao, Activating MoS $_2$ for pH-Universal Hydrogen Evolution Catalysis, J. Am. Chem. Soc. 139 (2017) 16194–16200, https://doi.org/10.1021/jacs.7b07450.

[8] J. Jiang, M. Gao, W. Sheng, Y. Yan, Hollow Chevrel-Phase NiMo $_3$ S $_4$ for Hydrogen Evolution in Alkaline Electrolytes, Angew. Chem. 128 (2016) 15466–15471, https://doi.org/10.1002/ange.201607651.

[9] K. Zhang, Y. Duan, N. Graham, W. Yu, Unveiling the synergy of polymorph heterointerface and sulfur vacancy in NiS/Ni3S2 electrocatalyst to promote alkaline hydrogen evolution reaction, Appl. Catal. B 323 (2023), 122144, https://doi.org/10.1016/j.apcatb.2022.122144.

[10] Y. Wu, F. Li, W. Chen, Q. Xiang, Y. Ma, H. Zhu, et al., Coupling Interface Constructions of MoS $_2$ /Fe $_5$ Ni $_4$ S $_8$ Heterostructures for Efficient Electrochemical Water Splitting, Adv. Mater. 30 (2018) 1803151, https://doi.org/10.1002/adma.201803151.

[11] L. Xiao, P. Yao, T. Xue, F. Li, One-step electrodeposition synthesis of Ni/NiS @NF catalyst on nickel foam (NF) for hydrogen evolution reaction, Mol. Catal. 511 (2021), 111694, https://doi.org/10.1016/j.mcat.2021.111694.

[12] H. Öztürk Doğan, U.B. Kurt, NiS@CuBi2O4/ERGO heterostructured electrocatalyst for enhanced hydrogen evolution reaction, Micro Nanostruct. 183 (2023), 207666, https://doi.org/10.1016/j.micrna.2023.207666.

[13] C. Yan, J. Huang, C. Wu, Y. Li, Y. Tan, L. Zhang, et al., In-situ formed NiS/Ni coupled interface for efficient oxygen evolution and hydrogen evolution, J. Mater. Sci. Technol. 42 (2020) 10–16, https://doi.org/10.1016/j.jmst.2019.08.042.

[14] J. Jiang, M. Gao, W. Sheng, Y. Yan, Hollow Chevrel-Phase NiMo $_3$ S $_4$ for Hydrogen Evolution in Alkaline Electrolytes, Angew. Chem. Int. Ed. 55 (2016) 15240–15245, https://doi.org/10.1002/anie.201607651.

[15] H. He, H. Liu, F. Liu, K. Zhou, Structures and electrochemical properties of amorphous nickel sulphur coatings electrodeposited on the nickel foam substrate as hydrogen evolution reaction cathodes, Surf. Coat. Technol. 201 (2006) 958–964, https://doi.org/10.1016/j.surfcoat.2006.01.016.

[16] T.N.J.I. Edison, R. Atchudan, N. Karthik, K. Ganesh, D. Xiong, Y.R. Lee, A novel binder-free electro-synthesis of hierarchical nickel sulfide nanostructures on nickel foam as a battery-type electrode for hybrid-capacitors, Fuel 276 (2020), 118077, https://doi.org/10.1016/j.fuel.2020.118077.

[17] N.K. Chaudhari, H. Jin, B. Kim, K. Lee, Nanostructured materials on 3D nickel foam as electrocatalysts for water splitting, Nanoscale 9 (2017) 12231–12247, https://doi.org/10.1039/C7NR04187J.

[18] E. Prates da Costa, A. Hofmann, U. Göbel, P. Cop, B.M. Smarsly, Development of Pore Morphology During Nitrate Group Removal by Calcination of Mesoporous Ce x Zr 1−x-y-z Y y La z O 2−δ Powders, Langmuir 38 (2022) 8342–8352, https://doi.org/10.1021/acs.langmuir.2c00875.

[19] E. Özkan, A. Hofmann, M. Votsmeier, W. Wang, X. Huang, C. Kübel, et al., Comprehensive Characterization of a Mesoporous Cerium Oxide Nanomaterial with High Surface Area and High Thermal Stability, Langmuir 37 (2021) 2563–2574, https://doi.org/10.1021/acs.langmuir.0c02747.

[20] I.A. Poimenidis, M. Lykaki, S. Moustaizis, P. Loukakos, M. Konsolakis, One-step solvothermal growth of NiO nanoparticles on nickel foam as a highly efficient electrocatalyst for hydrogen evolution reaction, Mater. Chem. Phys. 305 (2023), 128007, https://doi.org/10.1016/j.matchemphys.2023.128007.

[21] Yu Y. Study on Electrochemistry and Nucleation Process of Nickel Electrodeposition. Int. J. Electrochem. Sci. 2017:485–95. 10.20964/2017.01.48.

[22] J. Shi, X. Li, G. He, L. Zhang, M. Li, Electrodeposition of high-capacitance 3D CoS/graphene nanosheets on nickel foam for high-performance aqueous asymmetric supercapacitors, J Mater Chem A Mater 3 (2015) 20619–20626, https://doi.org/10.1039/C5TA04464B.

[23] A. Irshad, N. Munichandraiah, Electrodeposited Nickel–Cobalt–Sulfide Catalyst for the Hydrogen Evolution Reaction, ACS Appl. Mater. Interfaces 9 (2017) 19746–19755, https://doi.org/10.1021/acsami.6b15399.

[24] J.-Y. Lin, J.-H. Liao, S.-W. Chou, Cathodic electrodeposition of highly porous cobalt sulfide counter electrodes for dye-sensitized solar cells, Electrochim. Acta 56 (2011) 8818–8826, https://doi.org/10.1016/j.electacta.2011.07.080.

[25] J. Zhang, C. Xu, D. Zhang, J. Zhao, S. Zheng, H. Su, et al., Facile Synthesis of a Nickel Sulfide (NiS) Hierarchical Flower for the Electrochemical Oxidation of H 2 O 2 and the Methanol Oxidation Reaction (MOR), J. Electrochem. Soc. 164 (2017) B92–B96, https://doi.org/10.1149/2.0221704jes.

[26] S. Liu, Q. Shi, J. Tong, S. Li, M. Li, Controlled synthesis of spherical α-NiS and urchin-like β-NiS microstructures, J. Exp. Nanosci. 9 (2014) 475–481, https://doi.org/10.1080/17458080.2012.669853.

[27] T. Gao, M. Nie, J. Luo, Z. Huang, H. Sun, P. Guo, et al., Nickel sulfides supported by carbon spheres as efficient catalysts for hydrogen evolution reaction, Electrochem. Commun. 129 (2021), 107076, https://doi.org/10.1016/j.elecom.2021.107076.

[28] Y. Yu, S.J. Lee, J. Theerthagiri, Y. Lee, M.Y. Choi, Architecting the AuPt alloys for hydrazine oxidation as an anolyte in fuel cell: Comparative analysis of hydrazine splitting and water splitting for energy-saving H2 generation, Appl. Catal. B 316 (2022), 121603, https://doi.org/10.1016/j.apcatb.2022.121603.

[29] R. Chattot, T. Asset, P. Bordet, J. Drnec, L. Dubau, F. Maillard, Beyond Strain and Ligand Effects: Microstrain-Induced Enhancement of the Oxygen Reduction Reaction Kinetics on Various PtNi/C Nanostructures, ACS Catal. 7 (2017) 398–408, https://doi.org/10.1021/acscatal.6b02356.

[30] G. Greczynski, L. Hultman, X-ray photoelectron spectroscopy: Towards reliable binding energy referencing, Prog. Mater Sci. 107 (2020), 100591, https://doi.org/10.1016/j.pmatsci.2019.100591.

[31] T. Brousse, D. Bélanger, J.W. Long, To Be or Not To Be Pseudocapacitive? J. Electrochem. Soc. 162 (2015) A5185–A5189, https://doi.org/10.1149/2.0201505jes.

[32] Z. Xing, Q. Chu, X. Ren, C. Ge, A.H. Qusti, A.M. Asiri, et al., Ni3S2 coated ZnO array for high-performance supercapacitors, J. Power Sources 245 (2014) 463–467, https://doi.org/10.1016/j.jpowsour.2013.07.012.

[33] Z. Zhang, C. Zhao, S. Min, X. Qian, A facile one-step route to RGO/Ni3S2 for high-performance supercapacitors, Electrochim. Acta 144 (2014) 100–110, https://doi.org/10.1016/j.electacta.2014.08.038.

[34] Y. Li, K. Ye, K. Cheng, J. Yin, D. Cao, G. Wang, Electrodeposition of nickel sulfide on graphene-covered make-up cotton as a flexible electrode material for high-performance supercapacitors, J. Power Sources 274 (2015) 943–950, https://doi.org/10.1016/j.jpowsour.2014.10.156.

[35] X. Yin, G. Sun, A. Song, L. Wang, Y. Wang, H. Dong, et al., A novel structure of Ni-(MoS 2 /GO) composite coatings deposited on Ni foam under supergravity field as efficient hydrogen evolution reaction catalysts in alkaline solution, Electrochim. Acta 249 (2017) 52–63, https://doi.org/10.1016/j.electacta.2017.08.010.

[36] A.R. Neale, Y. Jin, J. Ouyang, S. Hughes, D. Hesp, V. Dhanak, et al., Electrochemical performance of laser micro-structured nickel oxyhydroxide cathodes, J. Power Sources 271 (2014) 42–47, https://doi.org/10.1016/j.jpowsour.2014.07.167.

[37] H. Huang, X. Deng, L. Yan, G. Wei, W. Zhou, X. Liang, et al., One-Step Synthesis of Self-Supported Ni3S2/NiS Composite Film on Ni Foam by Electrodeposition for High-Performance Supercapacitors, Nanomaterials 9 (2019) 1718, https://doi.org/10.3390/nano9121718.

[38] H. Jing, M. You, S. Yi, T. Li, H. Ji, Y. Wang, et al., Precursor-Engineering Coupled Microwave Molten-Salt Strategy Enhances Photocatalytic Hydrogen Evolution Performance of g-C 3 N 4 Nanostructures, ChemSusChem 13 (2020) 827–837, https://doi.org/10.1002/cssc.201902730.

[39] Z. Jin, P. Li, X. Huang, G. Zeng, Y. Jin, B. Zheng, et al., Three-dimensional amorphous tungsten-doped nickel phosphide microsphere as an efficient electrocatalyst for hydrogen evolution, J. Mater. Chem. A 2 (2014) 18593–18599, https://doi.org/10.1039/C4TA04434G.

[40] L. Liao, J. Zhu, X. Bian, L. Zhu, M.D. Scanlon, H.H. Girault, et al., MoS $_2$ Formed on Mesoporous Graphene as a Highly Active Catalyst for Hydrogen Evolution, Adv. Funct. Mater. 23 (2013) 5326–5333, https://doi.org/10.1002/adfm.201300318.

[41] W. Zhang, D. Li, L. Zhang, X. She, D. Yang, NiFe-based nanostructures on nickel foam as highly efficiently electrocatalysts for oxygen and hydrogen evolution reactions, J. Energy Chem. 39 (2019) 39–53, https://doi.org/10.1016/j.jechem.2019.01.017.

[42] W.-F. Chen, J.T. Muckerman, E. Fujita, Recent developments in transition metal carbides and nitrides as hydrogen evolution electrocatalysts, Chem. Commun. 49 (2013) 8896, https://doi.org/10.1039/c3cc44076a.

[43] A.P. Murthy, J. Theerthagiri, J. Madhavan, Insights on Tafel Constant in the Analysis of Hydrogen Evolution Reaction, J. Phys. Chem. C 122 (2018) 23943–23949, https://doi.org/10.1021/acs.jpcc.8b07763.

[44] Y. An, B. Huang, Z. Wang, X. Long, Y. Qiu, J. Hu, et al., Constructing three-dimensional porous Ni/Ni $_3$ S 2 nano-interfaces for hydrogen evolution electrocatalysis under alkaline conditions, Dalton Trans. 46 (2017) 10700–10706, https://doi.org/10.1039/C7DT00878C.

[45] I.A. Poimenidis, N. Papakosta, A. Manousaki, A. Klini, M. Farsari, S.D. Moustaizis, et al., Electrodeposited laser – nanostructured electrodes for increased hydrogen production, Int. J. Hydrogen Energy 47 (2022) 9527–9536, https://doi.org/10.1016/J.IJHYDENE.2022.01.062.

[46] I.A. Poimenidis, M.D. Tsanakas, N. Papakosta, A. Klini, M. Farsari, S.D. Moustaizis, et al., Enhanced hydrogen production through alkaline electrolysis using laser-nanostructured nickel electrodes, Int. J. Hydrogen Energy 46 (2021) 37162–37173, https://doi.org/10.1016/j.ijhydene.2021.09.010.

[47] D.M. Morales, M. Risch, Seven steps to reliable cyclic voltammetry measurements for the determination of double layer capacitance, J. Phys.: Energy 3 (2021), 034013, https://doi.org/10.1088/2515-7655/abee33.

[48] H. Wang, L. Pilon, Physical interpretation of cyclic voltammetry for measuring electric double layer capacitances, Electrochim. Acta 64 (2012) 130–139, https://doi.org/10.1016/j.electacta.2011.12.118.

[49] Chandrasekaran P, Nesakumar Jebakumar Immanuel Edison T, Gopalakrishnan Sethuraman M. Electrocatalytic study of carbon dots/ Nickel iron layered double hydroxide composite for oxygen evolution reaction in alkaline medium. Fuel 2022; 320:123947. 10.1016/j.fuel.2022.123947.

[50] S.I. Perez Bakovic, P. Acharya, M. Watkins, H. Thornton, S. Hou, L.F. Greenlee, Electrochemically active surface area controls HER activity for FexNi100−x films in alkaline electrolyte, J. Catal. 394 (2021) 104–112, https://doi.org/10.1016/j.jcat.2020.12.037.

[51] I.A. Poimenidis, N. Papakosta, A. Klini, M. Farsari, M. Konsolakis, P.A. Loukakos, et al., Electrodeposited Ni foam electrodes for increased hydrogen production in alkaline electrolysis, Fuel 342 (2023), 127798, https://doi.org/10.1016/j.fuel.2023.127798.

[52] E. Navarro-Flores, Z. Chong, S. Omanovic, Characterization of Ni, NiMo, NiW and NiFe electroactive coatings as electrocatalysts for hydrogen evolution in an acidic medium, J. Mol. Catal. A Chem. 226 (2005) 179–197, https://doi.org/10.1016/j.molcata.2004.10.029.

[53] X. Li, P.F. Liu, L. Zhang, M.Y. Zu, Y.X. Yang, H.G. Yang, Enhancing alkaline hydrogen evolution reaction activity through Ni-Mn3O4 nanocomposites, Chem. Commun. 52 (2016) 10566–10569, https://doi.org/10.1039/C6CC04141H.

[54] N.K. Shrestha, S.A. Patil, J. Han, S. Cho, A.I. Inamdar, H. Kim, et al., Chemical etching induced microporous nickel backbones decorated with metallic Fe@ hydroxide nanocatalysts: an efficient and sustainable OER anode toward industrial

alkaline water-splitting, J Mater Chem A Mater 10 (2022) 8989–9000, https://doi.org/10.1039/D1TA10103J.
[55] Y. Zhang, H. Feng, X. Wu, L. Wang, A. Zhang, T. Xia, et al., Progress of electrochemical capacitor electrode materials: A review, Int. J. Hydrogen Energy 34 (2009) 4889–4899, https://doi.org/10.1016/j.ijhydene.2009.04.005.
[56] D. Chinnadurai, R. Rajendiran, O.L. Li, K. Prabakar, Mn-Co bimetallic phosphate on electrodeposited PANI nanowires with composition modulated structural morphology for efficient electrocatalytic water splitting, Appl. Catal. B 292 (2021), 120202, https://doi.org/10.1016/j.apcatb.2021.120202.
[57] Y. Yu, S.J. Lee, J. Theerthagiri, S. Fonseca, L.M.C. Pinto, G. Maia, et al., Reconciling of experimental and theoretical insights on the electroactive behavior of C/Ni nanoparticles with AuPt alloys for hydrogen evolution efficiency and Non-enzymatic sensor, Chem. Eng. J. 435 (2022), 134790, https://doi.org/10.1016/j.cej.2022.134790.
[58] J. Chen, Z. Wang, J. Mu, B. Ai, T. Zhang, W. Ge, et al., Enhanced lithium storage capability enabled by metal nickel dotted NiO–graphene composites, J. Mater. Sci. 54 (2019) 1475–1487, https://doi.org/10.1007/s10853-018-2882-3.
[59] S.-E.-T. Siddiqui, M.A. Rahman, J.-H. Kim, S.S. Bin, S. Paul, A Review on Recent Advancements of Ni-NiO Nanocomposite as an Anode for High-Performance Lithium-Ion Battery, Nanomaterials (2022;12:2930.), https://doi.org/10.3390/nano12172930.
[60] X. Chia, A. Ambrosi, Z. Sofer, J. Luxa, M. Pumera, Catalytic and Charge Transfer Properties of Transition Metal Dichalcogenides Arising from Electrochemical Pretreatment, ACS Nano 9 (2015) 5164–5179, https://doi.org/10.1021/acsnano.5b00501.
[61] B.E. Conway, V. Birss, J. Wojtowicz, The role and utilization of pseudocapacitance for energy storage by supercapacitors, J. Power Sources 66 (1997) 1–14, https://doi.org/10.1016/S0378-7753(96)02474-3.
[62] P. Chulkin, P. Data, Electrochemical Impedance Spectroscopy as a Tool for Electrochemical Rate Constant Estimation, J. Vis. Exp. (2018), https://doi.org/10.3791/56611.
[63] Y. Zhang, L. Lin, J. Liu, J. Peng, Z. Chen, L. Chen, A hierarchical and branch-like NiCoS/NF material prepared by gradient electrodeposition method for oxygen evolution reaction, Int. J. Hydrogen Energy 46 (2021) 36629–36639, https://doi.org/10.1016/j.ijhydene.2021.08.187.
[64] R.K. Shervedani, A.R. Madram, Kinetics of hydrogen evolution reaction on nanocrystalline electrodeposited Ni62Fe35C3 cathode in alkaline solution by electrochemical impedance spectroscopy, Electrochim. Acta 53 (2007) 426–433, https://doi.org/10.1016/j.electacta.2007.06.006.